

Finite Thickness Effects on Metallization Vs. Chiral Majorana Fermions

Xin Yue,¹ Guo-Jian Qiao,^{1,2,*} and C. P. Sun^{2,†}

¹Beijing Computational Science Research Center, Beijing 100193, China

²Graduate School of China Academy of Engineering Physics, Beijing 100193, China

In heterostructures composed of quantum anomalous Hall insulators and s -wave superconductors (SCs), metallization hinders the identification of chiral Majorana fermions (CMFs). In this Letter, we study how the thickness of SC affects the competition between metallization and CMFs by a holistic approach previously developed for hybrid nanowire systems [Phys. Rev. Lett. 133, 266605 (2024)]. We predict three types of structures that vary with thickness of SC: (i) Periodic structure of metallization. For thin SCs (~ 10 nm), the metallization region exhibits oscillations as the thickness of SC changes, with the oscillation period corresponding to the Fermi wavelength of SC. (ii) Periodic structure of CMFs. For intermediate thicknesses (~ 100 nm), the window width for observing CMFs exhibits a periodic behavior, oscillating with the same period. (iii) Stable structure of CMFs. For thick SCs (~ 1000 nm), the behavior of CMFs becomes uniform as the thickness varies. Optimizing the thickness of SC may thus improve data quality and provide clearer evidence for CMFs.

Introduction—The pursuit of Majorana fermions in condensed matter systems over the past two decades has been fueled by their non-Abelian statistics and potential applications in topological quantum computing [1–5]. Although theoretical proposals for chiral Majorana fermions (CMFs) in heterostructures composed of quantum anomalous Hall (QAH) insulators proximity-coupled s -wave superconductors (SCs) have long been proposed [6–10], experiments about CMFs remains contentious [11–17]. It was found that metallization effects (SC layer makes the QAH insulator metallic) can produce spurious signatures, which further hinder the identification of CMFs [13, 15, 16, 18].

Recent experiments observations suggest that the metallization depends heavily on the proximity coupling strength, and it occurs under strong proximity coupling [16, 18]. However, earlier theories of CMFs in heterostructures [7–10] were typically based on phenomenological models, which assumed that the electron pairing is always induced by superconducting proximity effect. However, by eliminating quasi-excitations in SC [19, 20], it has been demonstrated that these oversimplified models only work well under weak proximity coupling conditions [20]. In this sense, the existing theory cannot describe CMFs in the strong proximity coupling and metallization effect. Therefore, we need to develop a microscopic theory for CMFs that is applicable under arbitrary proximity coupling strength, and further determines whether metallization will occur to block the emergence of CMFs.

In addition, the thickness of the SC layers used in experiments ranges from 50 nm to 350 nm [11, 16, 17], which falls within the mesoscopic scale—an intermediate regime between two-dimensional (2D) and three-dimensional (3D) systems. To our best knowledge, this finite-thickness effects of SC [21] on the experimental observation of CMFs has not yet been considered. Thus,

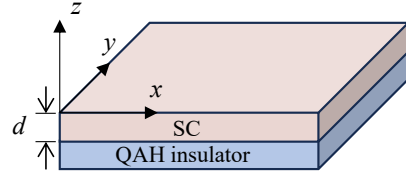


FIG. 1. Heterostructure composed of a superconductor (SC) layer with thickness d layered atop a Quantum Anomalous Hall (QAH) insulator layer.

it is essential to account for this effect and offer precise guidance on choosing the superconducting layer thickness for the observation of CMFs.

In this Letter, we utilize a minimal microscopic model of a QAH insulator coupled to a 2D superconductor to explore the effects of proximity coupling strength on CMFs. We introduce the concept of dressed CMFs by extending the theoretical framework of dressed Majorana fermions from 1D hybrid systems [22, 23] to our 2D case. The dressed CMFs incorporate excitations of both the QAH insulator and the SC. We demonstrate that metallization arises from a characteristic chemical potential shift combined with a nearly vanishing induced gap. Crucially, for realistic material parameters, the metallization region overlaps with the domain hosting $\mathcal{N} = 1$ dressed CMFs, posing a significant challenge for experimental observation.

Incorporating the finite-thickness effect of SC into our analysis, we reveal three main findings: (i) For thin SCs (~ 10 nm), there is a periodic structure of metallization with a period corresponding to the SC's Fermi wavelength, and metallization typically occurs except near resonance thicknesses. The periodicity originates from the fact that band shifts and proximity-induced gaps oscillate with the SC's thickness. This oscillatory behavior was also reported in semiconductor nanowire/SC systems [21, 24], highlighting the importance of precise thickness control. (ii) For intermediate thicknesses (~ 100 nm), the window width for observing CMF signals ex-

* qiaogj0211@csrc.ac.cn

† suncp@gscaep.ac.cn

hibits periodic behavior, oscillating at the Fermi wavelength. The observation window is significantly widened when the thickness reaches resonance points. (iii) For thick SCs (~ 1000 nm), the behavior of CMFs becomes uniform as the thickness varies, with the proximity-induced gap remaining stable. While thicker SCs generally enhance the proximity effect, precise thickness control for intermediate thicknesses near resonance points can dramatically increase the induced gap, effectively suppress metallization, and significantly widen the observation window for CMF signals.

Majorana in microscopic model—In previous studies, a quantum anomalous Hall (QAH) insulator (such as Cr- or Fe-doped Bi_2Se_3) coupled to a SC is described by phenomenological theory and its Hamiltonian in Nambu representation reads [8, 9]:

$$\mathcal{H}_P(\mathbf{k}) = \begin{pmatrix} h_Q(\mathbf{k}) - \mu & i\Delta\sigma_y \\ -i\Delta\sigma_y & -h_Q^*(-\mathbf{k}) + \mu \end{pmatrix}, \quad (1)$$

where the two-band model of QAH insulator is

$$h_Q(\mathbf{k}) = A(k_x\sigma_x + k_y\sigma_y) + (m + Bk^2)\sigma_z. \quad (2)$$

Here, A is the Fermi velocity, m denotes the mass gap, B represents the parabolic term and $\sigma_{x,y,z}$ are Pauli matrices. μ is the chemical potential and Δ is the pairing strength. To our best knowledge, the dependence of Δ and μ on microscopic parameters, such as proximity coupling strength and superconducting gap, is unclear in this phenomenological approach [5, 19, 20].

To determine the microscopic representations of Δ and μ in terms of practical parameters, we study the holistic Hamiltonian of the QAH-SC system: $H = H_Q + H_{\text{SC}} + H_T$, where

$$H_Q = \int \frac{d^2k}{(2\pi)^2} \boldsymbol{\varphi}_{\mathbf{k}}^\dagger [h_Q(\mathbf{k}) - \mu_m] \boldsymbol{\varphi}_{\mathbf{k}}. \quad (3)$$

Here, $\boldsymbol{\varphi}_{\mathbf{k}} = [\varphi_{\mathbf{k}\uparrow}, \varphi_{\mathbf{k}\downarrow}]^T$, and μ_m is the chemical potential of QAH insulator. The s -wave SC is described by Bardeen-Cooper-Schrieffer (BCS) Hamiltonian:

$$H_{\text{SC}} = \int \frac{d^2k}{(2\pi)^2} \mathbf{c}_{\mathbf{k}}^\dagger [\epsilon_s \sigma_z + \Delta_s \sigma_x] \mathbf{c}_{\mathbf{k}}, \quad (4)$$

where $\mathbf{c}_{\mathbf{k}} = [c_{\mathbf{k}\uparrow}, c_{\mathbf{k}\downarrow}]^T$ represents the Nambu spinor, $\epsilon_s = \hbar^2 \mathbf{k}^2 / (2m_s) - \mu_s$ is the kinetic energy above the Fermi level μ_s , m_s is the electron mass and Δ_s is the superconducting gap. The tunneling coupling between the QAH insulator and SC is:

$$H_T = T \int \frac{d^2k}{(2\pi)^2} \sum_{\sigma=\uparrow,\downarrow} \left[\varphi_{\mathbf{k}\sigma}^\dagger c_{\mathbf{k}\sigma} + \text{H.c.} \right]. \quad (5)$$

Here, we consider that the proximity coupling strength T is momentum independent and spin conservation is preserved during the tunneling process. Combining Eqs.

(3, 4, 5), the holistical Hamiltonian in the Nambu basis of $[\boldsymbol{\varphi}_{\mathbf{k}}, \mathbf{c}_{\mathbf{k}}, \boldsymbol{\varphi}_{-\mathbf{k}}^\dagger, \mathbf{c}_{-\mathbf{k}}^\dagger]^T$, is reexpressed as

$$\mathcal{H}(\mathbf{k}) = \begin{pmatrix} h(\mathbf{k}) & p \\ p^\dagger & -h^*(-\mathbf{k}) \end{pmatrix}, \quad h = \begin{pmatrix} h_Q - \mu_m & T \\ T & \epsilon_s \end{pmatrix}. \quad (6)$$

Here, $p = \text{diag}(\mathbf{0}, i\Delta_s \sigma_y)$ is a diagonal block matrix containing superconducting pairing.

To obtain the holistical edge state of CMFs in the spatial representation, we now solve the eigen-states of the holistic Hamiltonian with the periodic boundary condition in the x direction and an open boundary condition in the y direction. In this case, k_y is replaced by $-i\partial_y$, and the eigen equation becomes: $\mathcal{H}(k_x, -i\partial_y) \boldsymbol{\Psi}_{k_x}(y) = E(k_x) \boldsymbol{\Psi}_{k_x}(y)$, where $\boldsymbol{\Psi}_{k_x}(y) = [\mathbf{u}_{k_x}(y), \mathbf{v}_{k_x}(y)]^T$. The corresponding Bogoliubov quasi-excitation is

$$\gamma_{k_x}^\dagger = \int dy [\boldsymbol{\psi}_{k_x}^\dagger(y) \cdot \mathbf{u}_{k_x}(y) + \boldsymbol{\psi}_{-k_x}^T(y) \cdot \mathbf{v}_{k_x}(y)], \quad (7)$$

where $\mathbf{o}_{k_x} = [o_{m\uparrow}, o_{m\downarrow}, o_{s\uparrow}, o_{s\downarrow}]^T$ with $o(=u, v)$ respectively denotes eigen-wave function of the electron and hole, and $\boldsymbol{\psi}_{k_x}(y)$ is the Fourier transformation of $\boldsymbol{\psi}_{\mathbf{k}} = [\boldsymbol{\varphi}_{\mathbf{k}}, \mathbf{c}_{\mathbf{k}}]^T$ in y component. It follows from Eq. (7) that the operator that creates a quasiparticle at position x is $\gamma^\dagger(x) = \int dk_x \gamma_{k_x}^\dagger \exp(-ik_x x)$. Following the definition of the Majorana particle (its own antiparticle is itself), the field operator generates the Majorana mode if it satisfies $\gamma(x) = \gamma^\dagger(x)$. We name it a dressed CMF since it includes both electronic excitations from the QAH insulator and quasiexcitations from the SC [22]. By the definition of dressed CMF, we have $\gamma_{k_x}^\dagger = \gamma_{-k_x}$, and further this condition requires that $\mathbf{u}_{k_x}(y) = \mathbf{v}_{-k_x}^*(y)$.

Assume that the edge state of the dressed CMF propagates along the x -direction, while being localized at the edge in the y -direction: $\boldsymbol{\Psi}_{k_x}(y) = \exp(-\xi y) [\mathbf{u}_{k_x}, \mathbf{u}_{-k_x}^*]^T$. First, we consider the scenario where $E = 0$ and $k_x = 0$. In this case, a non-trivial solution exists if $\det[\mathcal{H}(0, i\xi)] = \sum_{n=0}^{16} c_n \xi^n = 0$. Here, the coefficient c_0 is given by $c_0 = [E_s^2(\mu_m^2 - m^2) + T^4 - 2T^2\mu_m\mu_s]^2$, where $E_s^2 = \Delta_s^2 + \mu_s^2$. The remaining coefficients are not relevant to the primary focus of our analysis. Since $\xi = 0$ corresponds to an infinite decay length, this condition $\det[\mathcal{H}(0, 0)] = c_0 = 0$ determines the phase boundary at which the holistic edge mode emerges or disappears. This phase boundary is obtained as:

$$m^2 = \Delta_{\text{eff}}^2 + \mu_{\text{eff}}^2 \quad (8)$$

with $\mu_{\text{eff}} = \mu_m + \text{Re}(\chi)$ and $\Delta_{\text{eff}} = \text{Im}(\chi)$, respectively. Here, $\chi = -T^2/(\mu_s + i\Delta_s)$ characterizes the dressed effect of the SC on the QAH insulator.

The number of Majorana edge states in three parameter regions—We consider a system of length L_y in the y -direction, with the wave function vanishing at the boundaries as required by physical constraints [25]: $\boldsymbol{\Psi}(y=0) = \boldsymbol{\Psi}(y=L_y) = 0$. For the specific case where $\mu_{\text{eff}} = 0$ and under the approximation that $\mu_s + \xi^2/(2m_s) \approx \mu_s$, the

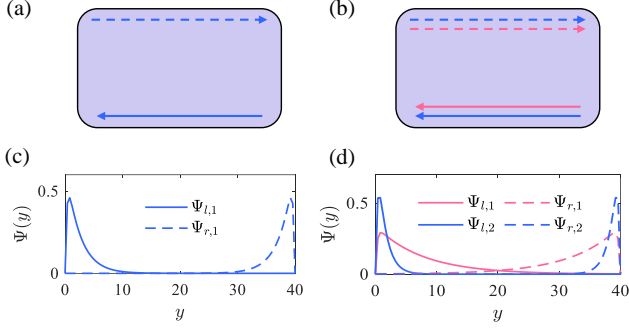


FIG. 2. (a,b) A schematic illustration of edge state distribution in the $x-y$ plane. The edge states near $y = 0$ propagate to the $+x$ direction, and the edge states near $y = L_y$ propagate to the $-x$ direction. (c,d) Edge state distribution in the y direction, which is plotted by the analytical solution of wave function Ψ . Only the first component of Ψ is plotted. The parameters are $\Delta_{\text{eff}} = 1$, $A = B = 1$ and $L_y = N_y a = 40$ with $a = 1$. The system exhibits one edge states ($\mathcal{N} = 1$) on each edge when $m = -0.5$ ($|m| < \Delta_{\text{eff}}$), as illustrated in panels (a) and (c). In contrast, it displays two edge state ($\mathcal{N} = 2$) on each edge for $m = -1.5$ ($m < -\Delta_{\text{eff}}$), as shown in panels (b) and (d). The edge states localized in left (right) are labeled by solid (dashed) lines.

state number of dressed CMFs is determined in three different regions of the parameter space (m, Δ_{eff}): (i) when $m > \Delta_{\text{eff}}$, no edge state exists; (ii) when $|m| < \Delta_{\text{eff}}$, there is only one edge state on each edge. These edge states are given by:

$$\begin{aligned} \Psi_{r,1}(y) &\propto \begin{pmatrix} \mathbf{u}_+ \\ \mathbf{u}_+ \end{pmatrix} \left(e^{-\xi_{+,1}(y-L_y)} - e^{-\xi_{-,1}(y-L_y)} \right), \\ \Psi_{l,1}(y) &\propto i \begin{pmatrix} \mathbf{u}_- \\ -\mathbf{u}_- \end{pmatrix} (e^{\xi_{+,1}y} - e^{\xi_{-,1}y}). \end{aligned} \quad (9)$$

Here, $\mathbf{u}_{\pm} = [\mp E_s^2, E_s^2, T(\Delta_s \mp \mu_s), T(\mu_s \pm \Delta_s)]^T$ are the coefficient vectors and $\xi_{\pm,1} = (-A \pm Q)/2B$ are the decay factors with $Q = \sqrt{A^2 - 4B(\Delta_{\text{eff}} - m)}$; The solutions $\Psi_{r,1}(y)$ and $\Psi_{l,1}(y)$ are invalid when $m > \Delta_{\text{eff}}$ because, in this case, the decay factors $\xi_{+,1}$ and $\xi_{-,1}$ have opposite signs, making it impossible to simultaneously satisfy the boundary conditions at both edges. (iii) when $m < -\Delta_{\text{eff}}$, there are two edge states on each edge. In addition to $\Psi_{l,1}$ and $\Psi_{r,1}$, the other two edge states are $\Psi_{l,2}$ and $\Psi_{r,2}$. The explicit forms of $\Psi_{l,2}$ and $\Psi_{r,2}$ are similar to Eq. (9), with details provided in Appendix A of the End Matter.

When $k_x \neq 0$ (k_x is small), we employ degenerate perturbation theory by taking the perturbation Hamiltonian as: $\mathcal{H}_1(k_x) = \mathcal{H}(k_x, i\xi) - \mathcal{H}(0, i\xi)$. As $|m| < \Delta_{\text{eff}}$, in the degenerate space spanned by $\{\Psi_{l,1}, \Psi_{r,1}\}$, the perturbation Hamiltonian is diagonal:

$$H_1 \doteq Z \begin{bmatrix} Ak_x & 0 \\ 0 & -Ak_x \end{bmatrix}. \quad (10)$$

Here, $Z = \Delta_s/(\Delta_s + \Delta_{\text{eff}})$ is the renormalization factor. The energy spectrum is linear in k_x , indicating a massless edge quasi-particle with renormalized group velocity ZA/\hbar . The edge state near $y = 0$ ($\Psi_{l,1}$) propagates exclusively in the $+x$ direction, while the edge state near $y = L_y$ ($\Psi_{r,1}$) propagates exclusively in the $-x$ direction [see Fig. 2(a,c)]. This behavior is characteristic of chirality [6]. The case for $m < -\Delta_{\text{eff}}$ can be analyzed similarly, with the corresponding results shown in Fig. 2(b,d).

Without crossing a phase boundary given by Eq. (8), the number of edge states remains the same. Therefore, we can extrapolate the results for $\mu_{\text{eff}} = 0$ to obtain the distribution of edge states across the entire parameter space:

$$\mathcal{N} = \begin{cases} 0, & m > \sqrt{\Delta_{\text{eff}}^2 + \mu_{\text{eff}}^2}, \\ 1, & |m| < \sqrt{\Delta_{\text{eff}}^2 + \mu_{\text{eff}}^2}, \\ 2, & m < -\sqrt{\Delta_{\text{eff}}^2 + \mu_{\text{eff}}^2}. \end{cases} \quad (11)$$

This result is consistent with the the topological phase region determined by computing the Chern number, which captures the bulk-edge correspondence [26]. It seems the same as the outcome obtained earlier in Refs. [8, 9], where the phase boundary is defined as $m^2 = \Delta^2 + \mu^2$. Notably, in our findings, μ_{eff} and Δ_{eff} are not independent parameters, as they both depend on the proximity coupling strength T . Additionally, a significant shift $\text{Re}(\chi)$ in the chemical potential is observed, which increases with proximity coupling strength.

Metallization from chemical potential shift—According to band theory, metal is defined when the Fermi level situated in band and the system is gapless or the gap is very tiny. Therefore, when the chemical potential is shifted, the system may be render into metal. To illustrate metallization effect caused by the shift of the chemical potential, we compute the energy spectrum of holistic model (6). Specifically, we discretize the continuum model onto a square lattice model, and then compute the energy bands with periodic (open) boundary along the x (y) direction [8]. Considering the practical parameters of the QAH-SC heterostructure, $\mu_m = 0$ meV, $\mu_s = 5$ eV, $\Delta_s = 1.5$ meV, $T = 100$ meV, $A = 3$ eV Å, and $B = 15$ eV Å² [27–29], the computing results are presented in Fig. 3(a-d). As illustrated in Fig. 3(a), when $\mathcal{N} = 2$, two edge states are well-protected by the bulk gap. As m enters into the $\mathcal{N} = 1$ region, the bulk gap becomes very small, only a few microvolts, and the edge mode is submerged by the bulk state, as shown in Fig. 3(b, d). Consequently, the hybrid system behaves like a metal. When $\mathcal{N} = 0$, the gap is large with no edge state, indicating a normal insulator state [see Fig. 3(c)].

To visualize the metallization region, other parameters are set constant while T and m are varied. The band gap $E_{\text{gap}}(T, m)$ is obtained numerically by identifying the minimum energy point of the model (6) with periodic boundary conditions applied in both the x and y directions. It can be seen from Fig. 3 (e,f) that the

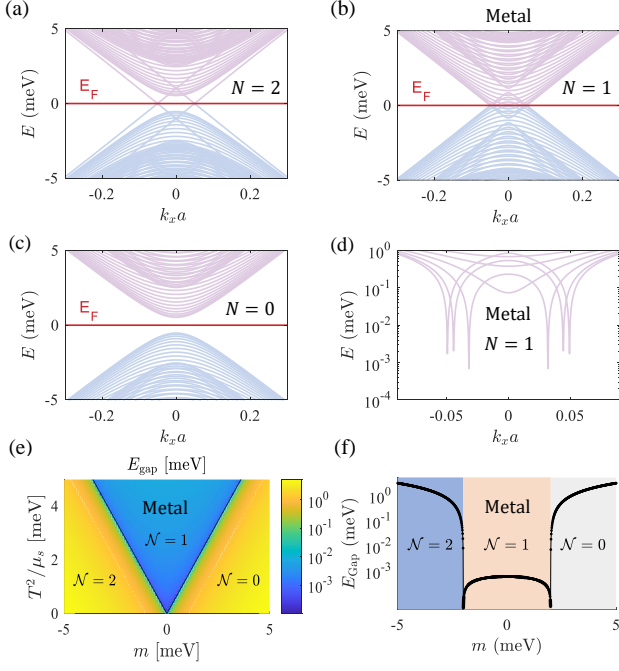


FIG. 3. Energy spectrum of the holistic Hamiltonian with periodic boundary conditions in the x direction and open boundary conditions in the y direction. The parameters are set as follows: $\mu_m = 0$, $\mu_s = 5$ eV, $m_s = 9.1 \times 10^{-31}$ kg, $\Delta_s = 1.5$ meV, $T = 100$ meV, $A = 3$ eVÅ, and $B = 15$ eVÅ², with a lattice constant $a = 7.5$ nm and a length $L_y = N_y a = 1.5$ μm along the y direction. Subplots (a-c) depict different values of the parameter m : (a) $m = -3$ meV, (b) $m = 0$ meV, and (c) $m = 3$ meV, corresponding to regions $\mathcal{N} = 2$, $\mathcal{N} = 1$, and $\mathcal{N} = 0$, respectively. (d) illustrates the metallization effect, while (e) is an enlarged view of (b), highlighting the tiny gap at the micro-electronvolt scale. (e) Energy gap as a function of T and m , denoted as $E_{\text{gap}}(m, T)$. The color scale represents the E_{gap} in meV, with regions labeled $\mathcal{N} = 0, 1, 2$ indicating different topological phases. (f) Energy gap as a function of m under the condition $T = 100$ meV. The color represent different topological regeion. The parameters used in (e) and (f) are the same as those in (a).

energy gap is nearly zero within the region $\mathcal{N} = 1$ ($|m| < T^2/\sqrt{\Delta_s^2 + \mu_s^2}$). Therefore, the metallization regions almost correspond to the $\mathcal{N} = 1$ region, which might also cause the half-integer signature, thus hindering the definitive identification of CMFs.

Crossover from 2D superconductor to 3D—In this section, we study the dependence of metallization on the thickness of SC so that the above 2D approach for CMF transfer to a more realistic 3D system. We replace the momentum of Eq. (4) as $\mathbf{k} \rightarrow (\mathbf{k}, k_z)$. Here, $k_z = n\pi/d$, $n = 0, \pm 1, \pm 2, \dots$ is the discrete momentum resulting from the finite thickness in the z direction. Besides, the proximity tunneling between the 2D QAH

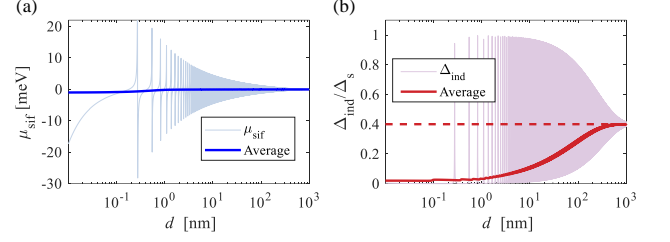


FIG. 4. (a) The chemical potential shift versus thickness of superconductor layer (light blue line). The dark blue line is the average of the light blue line. (b) Proximity-induced gap versus thickness of superconductor (ligh red line). The dark red line is an average of light red line. The dashed line is the analytical results in 3D limit when the superconductor is thick enough. The parameters are set as: $\mu_m = 0$, $\mu_s = 5$ eV, $m_s = 9.1 \times 10^{-31}$ kg, $\Delta_s = 1.5$ meV, $T^2 k_F = 10000$ [meV]² · [m]⁻¹.

insulator and the 3D SC is:

$$H_T = \sum_{k_z} T_{k_z} \int \frac{d^2 k}{(2\pi)^2} \sum_{\sigma=\uparrow, \downarrow} \left[\varphi_{\mathbf{k}\sigma}^\dagger c_{\mathbf{k}, k_z \sigma} + \text{H.c.} \right]. \quad (12)$$

Similarly, the topological phase boundary is obtained as [see Appendix B for details]

$$m^2 = \Delta_{\text{eff}}^2 + \mu_{\text{eff}}^2, \quad (13)$$

where $\mu_{\text{eff}} = \mu_m + \text{Re}(\chi)$ and $\Delta_{\text{eff}} = \text{Im}(\chi)$. The effective shift of the chemical potential and pairing strength depends on contributions from all subbands indicated by k_z :

$$\chi = \sum_{k_z} \frac{|T_{k_z}|^2}{\epsilon(k_z) - i\Delta_s}, \quad \epsilon(k_z) = \frac{\hbar^2 k_z^2}{2m_s} - \mu_s. \quad (14)$$

It follows from Eq. (13) that μ_{eff} and Δ_{eff} together determine the topological transition condition. Furthermore, they can directly establish a connection with observable quantities (the band shift μ_{sif} and proximity-induced gap Δ_{ind}) through a low-energy effective Hamiltonian [see Appendix C]: $\mu_{\text{sif}} = Z\mu_{\text{eff}}$ and $\Delta_{\text{ind}} = Z\Delta_{\text{eff}}$ [30, 31]. Here, $Z = \Delta_s/(\Delta_s + \Delta_{\text{eff}})$ is the renormalization factor, and Δ_{eff} characterizes the effective coupling strength: in the strong coupling regime ($\Delta_{\text{eff}} \gg \Delta_s$), $\Delta_{\text{ind}} \rightarrow \Delta_s$, while for weak coupling ($\Delta_{\text{eff}} \ll \Delta_s$), $\Delta_{\text{ind}} \approx \Delta_{\text{eff}}$.

For the case of homogeneous tunneling strength between the QAH insulator and 3D superconductor, $T_{k_z} = T/\sqrt{d}$, we calculate μ_{sif} and Δ_{ind} versus SC thickness d [Fig. 4(a,b)]. In the thin-SC limit ($d \ll \lambda_F$, with λ_F being the Fermi wavelength of SC), the contributions of higher subbands to the chemical potential shift are negligible. At this point, μ_{sif} and Δ_{ind} recover the results obtained by using 2D SC model. For thick-SC limit ($d \gg \xi_s$, where ξ_s is the coherence length of SC), the summation over k_z in Eq. (14) is converted into an integral. Consequently, we obtain $\mu_{\text{eff}} = 0$ and $\Delta_{\text{eff}} = (T^2/\hbar)\sqrt{m_s/2\mu_s}$ [2, 20], shown as the dashed line

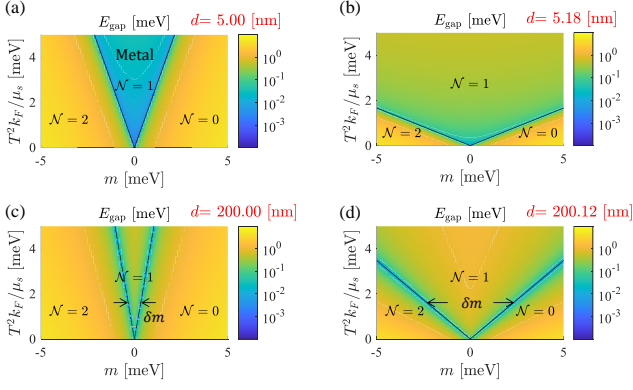


FIG. 5. Energy gap diagrams for various thicknesses d (a) $d = 5.00$ nm, (b) $d = 5.18$ nm, (c) $d = 200.00$ nm, and (d) $d = 200.12$ nm. Other parameters are set to be: $\mu_m = 0$, $\mu_s = 5$ eV, $m_s = 9.1 \times 10^{-31}$ kg, $\Delta_s = 1.5$ meV, $A = 3$ eVÅ, and $B = 15$ eVÅ².

in Fig. 4(b). When the SC thickness transitions between the 2D and 3D limits, the SC thickness dependence of μ_{eff} and Δ_{eff} exhibits oscillations at the SC Fermi wavelength scale. The peaks of the effective chemical potential and the induced pairing strength appear when $d \approx n\lambda_F/2$, n is integer. This phenomenon is attributed to the resonance between the Fermi surface and one of the subbands. Remarkably, thin superconducting layers, where resonances occur, can even induce larger gaps than those observed in thick-SC limit. The increased energy gap will expand the window for the appearance of signatures of CMFs ($0.5 e^2/h$), as discussed below.

To visualize the width of this window for observing CMF signatures, we compute the energy gap and the phase diagram as a function of superconductor thickness d (Fig. 5). At $d = 5$ nm, the phase diagram closely resembles the 2D SC case [Fig. 5(a) and 3(e)], where the $\mathcal{N} = 1$ region exhibits a tiny energy gap ($\sim \mu\text{eV}$) and behaves metallicity. When $d = 5.18$ nm (near the resonance point $d \simeq 19\lambda_F/2$), the induced gap approaches the SC bulk gap, shrinking the metallization region near phase boundaries [Fig. 5(b)].

The non-resonant thickness $d = 200.00$ nm produces a narrower signature window compared to the resonant case $d = 5.18$ nm [Fig. 5(b,c)]. Remarkably, a minor adjustment to $d = 200.12$ nm (near $732\lambda_F/2$) creates a broad signature window approximately 7 times wider than at $d = 200.00$ nm [Fig. 5(c,d)]. This sensitivity to thickness variations can be explained from Eq. (13): The

boundary condition $m = \pm\sqrt{\Delta_{\text{eff}}^2 + \mu_{\text{eff}}^2}$ determines the $\mathcal{N} = 1$ window width as $\delta m = 2\sqrt{\Delta_{\text{eff}}^2 + \mu_{\text{eff}}^2}$. Because both Δ_{eff} and μ_{eff} oscillate with d , the resulting δm exhibits strong thickness dependence.

Conclusion and Discussion—We developed a microscopic theory for chiral Majorana fermions (CMFs), which is suitable for arbitrary proximity coupling strength. We also systematically investigate how the finite thickness of the superconductor (SC) affects the detection of the CMF. There are three important findings: (i) Periodic structure of metallization. For thin SCs (~ 10 nm), the metallization region oscillates with the thickness of the superconductor, and its period corresponds to the Fermi wavelength of SC (λ_F). Metallization occurs except near resonance thicknesses where $d \approx n\lambda_F/2$. (ii) Periodic structure of CMFs. For intermediate thicknesses (~ 100 nm), the window width for observing CMFs changes periodically with the thickness of the superconductor. The oscillation period of this window is also λ_F . (iii) Stable structure of CMFs. For thick SCs (~ 1000 nm), the CMF shows uniform behavior as d varies. Metallization is absent in both (ii) and (iii). All these predictions regarding the thickness dependence can be experimentally verified.

Crucially, near resonance points ($d \approx n\lambda_F/2$), the induced gap can reach the SC gap, expanding the $\mathcal{N} = 1$ topological phase. This widens the mass gap range for observing the CMF signature ($0.5 e^2/h$). Given that experiments report half-integer plateaus only in narrow mass gap intervals, precise control of d could enhance the detectable range. Optimizing d may thus improve data quality and provide clearer evidence for CMFs.

Our analysis identifies two metallization criteria: substantial chemical potential shifts and ultra-small induced gaps ($\Delta_{\text{ind}} \sim \mu\text{eV}$). While the model handles arbitrary coupling strengths, unexplained metallization in strong-coupling regimes implies missing physics—likely from chemical potential inhomogeneity, interface structure, or non-ideal tunneling. These findings provide concrete guidelines for optimizing CMF platforms while highlighting the need for refined models of realistic heterostructures.

Acknowledgments—The authors appreciate quite much for the helpful discussion with Zhi-Lei Zhang and R. X. Zhai. This study is supported by the National Natural Science Foundation of China (NSFC) (Grant No. 12088101) and NSAF (Grants No. U2330401 and No. U2230402).

[1] A. Kitaev, Ann. Phys. **303**, 2 (2003).
[2] J. Alicea, Rep. Prog. Phys. **75**, 076501 (2012).
[3] C. Beenakker, Annu. Rev. Condens. Matter Phys. **4**, 113 (2013).
[4] K. Flensberg, F. von Oppen, and A. Stern, Nature Re-

views Materials **6**, 944 (2021).
[5] S.-W. Li, Z.-Z. Li, C. Y. Cai, and C. P. Sun, Phys. Rev. B **89**, 134505 (2014).
[6] N. Read and D. Green, Physical Review B **61**, 10267 (2000).

- [7] L. Fu and C. L. Kane, Phys. Rev. Lett. **100**, 096407 (2008).
- [8] X.-L. Qi, T. L. Hughes, and S.-C. Zhang, Phys. Rev. B **82**, 184516 (2010).
- [9] S. B. Chung, X.-L. Qi, J. Maciejko, and S.-C. Zhang, Phys. Rev. B **83**, 100512(R) (2011).
- [10] J. Wang, Q. Zhou, B. Lian, and S.-C. Zhang, Phys. Rev. B **92**, 064520 (2015).
- [11] Q. L. He, L. Pan, A. L. Stern, E. C. Burks, X. Che, G. Yin, J. Wang, B. Lian, Q. Zhou, E. S. Choi, *et al.*, Science **357**, 294 (2017).
- [12] D. Abergel, Nature Physics **16**, 123 (2020).
- [13] C.-Z. Chen, J. J. He, D.-H. Xu, and K. T. Law, Phys. Rev. B **96**, 041118 (2017).
- [14] Y. Huang, F. Setiawan, and J. D. Sau, Phys. Rev. B **97**, 100501 (2018).
- [15] W. Ji and X.-G. Wen, Phys. Rev. Lett. **120**, 107002 (2018).
- [16] Y. Huang, Y. Fu, P. Zhang, K. L. Wang, and Q. L. He, Journal of Physics: Condensed Matter **36**, 37LT01 (2024).
- [17] A. Uday, G. Lippertz, B. Bhujel, A. A. Taskin, and Y. Ando, Phys. Rev. B **111**, 035440 (2025).
- [18] M. Kayyalha, D. Xiao, R. Zhang, J. Shin, and C. Z. Chang, Science **367**, 64 (2020).
- [19] G.-J. Qiao, S.-W. Li, and C. P. Sun, Phys. Rev. B **106**, 104517 (2022).
- [20] X. Yue, G.-J. Qiao, and C. P. Sun, Phys. Rev. B **108**, 195405 (2023).
- [21] C. Reeg, D. Loss, and J. Klinovaja, Phys. Rev. B **96**, 125426 (2017).
- [22] G.-J. Qiao, X. Yue, and C. P. Sun, Phys. Rev. Lett. **133**, 266605 (2024).
- [23] Z.-L. Zhang, G.-J. Qiao, and C. P. Sun, arXiv preprint arXiv:2506.10367 (2025).
- [24] C. Reeg, D. Loss, and J. Klinovaja, Phys. Rev. B **97**, 165425 (2018).
- [25] B. Zhou, H.-Z. Lu, R.-L. Chu, S.-Q. Shen, and Q. Niu, Phys. Rev. Lett. **101**, 246807 (2008).
- [26] M. Z. Hasan and C. L. Kane, Rev. Mod. Phys. **82**, 3045 (2010).
- [27] C.-Z. Chen, Y.-M. Xie, J. Liu, P. A. Lee, and K. T. Law, Phys. Rev. B **97**, 104504 (2018).
- [28] Y. Zhang, K. He, C.-Z. Chang, C.-L. Song, L.-L. Wang, X. Chen, J.-F. Jia, Z. Fang, X. Dai, W.-Y. Shan, S.-Q. Shen, Q. Niu, X.-L. Qi, S.-C. Zhang, X.-C. Ma, and Q.-K. Xue, Nature Physics **6**, 584 (2010).
- [29] D. D. Miceli and L. Serra, Scientific Reports **13**, 19955 (2023).
- [30] T. D. Stanescu, J. D. Sau, R. M. Lutchyn, and S. Das Sarma, Phys. Rev. B **81**, 241310 (2010).
- [31] T. D. Stanescu and S. Das Sarma, Phys. Rev. B **96**, 014510 (2017).

End Matter

Appendix A—For the specific case where $\mu_{\text{eff}} = 0$ and under the approximation that $\mu_s + \xi^2/(2m_s) \approx \mu_s$, the determinant can be factored into the product of four terms:

$$\det[\mathcal{H}(0, i\xi)] = F_1 F_2 F_3 F_4,$$

where $F_1 = B\xi^2 + A\xi + \Delta_{\text{eff}} - m$, $F_2 = B\xi^2 - A\xi - \Delta_{\text{eff}} - m$, $F_3 = B\xi^2 - A\xi + \Delta_{\text{eff}} - m$, $F_4 = B\xi^2 + A\xi - \Delta_{\text{eff}} - m$.

Each quadratic corresponds to an equation in terms of ξ , whose solutions are:

$$\xi_{\pm,1} = \frac{-A \pm \sqrt{A^2 - 4B(\Delta_{\text{eff}} - m)}}{2B}, \quad \xi_{\pm,3} = -\xi_{\mp,1}$$

$$\xi_{\pm,2} = \frac{A \pm \sqrt{A^2 + 4B(\Delta_{\text{eff}} + m)}}{2B}, \quad \xi_{\pm,4} = -\xi_{\mp,2}$$

Each ξ is substituted into the eigenvalue equation to solve for specific values of the superposition coefficients \mathbf{u}, \mathbf{v} . By satisfying the open boundary conditions $\Psi(0) = \Psi(L_y) = 0$, each quadratic provides one solution, yielding a total of four solutions.

$$\Psi_{r,1}(y) = \frac{1}{\sqrt{A_m A_y}} \begin{pmatrix} \mathbf{u}_1 \\ \mathbf{u}_1 \end{pmatrix} (e^{-\xi_{+,1}(y-L_y)} - e^{-\xi_{-,1}(y-L_y)}),$$

$$\Psi_{r,2}(y) = \frac{i}{\sqrt{A_m A_y}} \begin{pmatrix} \mathbf{u}_1 \\ -\mathbf{u}_1 \end{pmatrix} (e^{\xi_{+,2}(y-L_y)} - e^{\xi_{-,2}(y-L_y)}),$$

$$\Psi_{l,1}(y) = \frac{i}{\sqrt{A_m A_y}} \begin{pmatrix} \mathbf{u}_2 \\ -\mathbf{u}_2 \end{pmatrix} (e^{\xi_{+,1}y} - e^{\xi_{-,1}y}),$$

$$\Psi_{l,2}(y) = \frac{1}{\sqrt{A_m A_y}} \begin{pmatrix} \mathbf{u}_2 \\ \mathbf{u}_2 \end{pmatrix} (e^{-\xi_{+,2}y} - e^{-\xi_{-,2}y}).$$

where

$$\mathbf{u}_1 = \begin{bmatrix} -\Delta_s^2 - \mu_s^2 \\ \Delta_s^2 + \mu_s^2 \\ T(\Delta_s - \mu_s) \\ T(\mu_s + \Delta_s) \end{bmatrix}, \quad \mathbf{u}_2 = \begin{bmatrix} \Delta_s^2 + \mu_s^2 \\ \Delta_s^2 + \mu_s^2 \\ T(\Delta_s + \mu_s) \\ T(\mu_s - \Delta_s) \end{bmatrix}.$$

The quantities $A_m = 2(\Delta_s^2 + \mu_s^2)(\Delta_s^2 + \mu_s^2 + T^2)$ and $A_y = \sqrt{A/(\Delta_{\text{eff}} - m) - B/A}$ are normalization coefficients for the \mathbf{u} -vector and the y -dependent function, respectively.

The parameter domain in which $\Psi_{r,1}(y)$ and $\Psi_{l,1}(y)$ are valid is $m < \Delta_{\text{eff}}$. This arises from the fact that when $m > \Delta_{\text{eff}}$, the decay factors $\xi_{+,1}$ and $\xi_{-,1}$ have opposite signs, making it impossible to satisfy the boundary conditions simultaneously. Conversely, for $m < \Delta_{\text{eff}}$, both $\xi_{+,1}$ and $\xi_{-,1}$ share the same sign (both being negative), allowing their linear combination to satisfy the boundary conditions at both ends consistently.

Similarly, for $\Psi_{r,2}(y)$ and $\Psi_{l,2}(y)$, the parameter domain in which they are valid is $m < -\Delta_{\text{eff}}$. When $m > \Delta_{\text{eff}}$, $\xi_{+,1}$ and $\xi_{-,1}$ have opposite signs, as do $\xi_{+,2}$ and $\xi_{-,2}$, meaning that no valid solution can be constructed under these circumstances.

The results are summarized in the table below:

	$\xi_{+,1}$	$\xi_{-,1}$	Solution	$\xi_{+,2}$	$\xi_{-,2}$	Solution
$m > \Delta_{\text{eff}}$	> 0	< 0	None	> 0	< 0	None
$ m < \Delta_{\text{eff}}$	< 0	< 0	$\Psi_{r,1}, \Psi_{l,1}$	> 0	< 0	None
$m < -\Delta_{\text{eff}}$	< 0	< 0	$\Psi_{r,1}, \Psi_{l,1}$	> 0	> 0	$\Psi_{r,2}, \Psi_{l,2}$

Appendix B—The tunneling Hamiltonian in real-space is:

$$H_1 = T \iint dx dy \sum_{\sigma=\uparrow,\downarrow} [\varphi_\sigma^\dagger(x, y) c_\sigma(x, y, 0) + \text{H.c.}]$$

We apply a Fourier transformation to this Hamiltonian, representing the field operators in momentum space as follows:

$$\varphi_\sigma(\mathbf{x}) = \int \frac{d^2 k}{(2\pi)^2} \varphi_{\mathbf{k}\sigma} e^{i\mathbf{k}\cdot\mathbf{x}}, \quad c_\sigma(\mathbf{x}, z) = \int \frac{d^2 k}{(2\pi)^2} c_{\mathbf{k}\sigma}(z) e^{i\mathbf{k}\cdot\mathbf{x}}$$

By substituting these expressions into the real-space Hamiltonian, we obtain the momentum-space representation:

$$H_T = T \int \frac{d^2 k}{(2\pi)^2} \sum_{\sigma=\uparrow,\downarrow} [\varphi_{\mathbf{k}\sigma}^\dagger c_{\mathbf{k}\sigma}(z=0) + \text{H.c.}]$$

To accommodate a finite size d , a discrete Fourier transform is performed in the z -direction:

$$c_{\mathbf{k}\sigma}(z) = \frac{1}{\sqrt{d}} \sum_{k_z} e^{ik_z z} c_{\mathbf{k}\sigma, k_z}$$

where $k_z = 2\pi n/d$. Consequently, the Hamiltonian becomes:

$$H_T = \sum_{k_z} T_{k_z} \int \frac{d^2 k}{(2\pi)^2} \sum_{\sigma=\uparrow,\downarrow} [\varphi_{\mathbf{k}\sigma}^\dagger c_{\mathbf{k}\sigma, k_z} + \text{H.c.}]$$

with $T_{k_z} = T/\sqrt{d}$. In the basis consisting of $[\varphi_{\mathbf{k}}, \varphi_{-\mathbf{k}}^\dagger, \mathbf{C}_{\mathbf{k}, k_{z_1}}, \mathbf{C}_{\mathbf{k}, k_{z_2}}, \dots, \mathbf{C}_{\mathbf{k}, k_{z_N}}]^T$, where each component $\mathbf{C}_{\mathbf{k}, k_z}$ is defined as $[\mathbf{c}_{\mathbf{k}, k_z}, \mathbf{c}_{-\mathbf{k}, k_z}^\dagger]^T$, the holistic Hamiltonian for the heterostructure is expressed as a block matrix:

$$\mathcal{H}(\mathbf{k}) = \begin{pmatrix} \mathcal{H}_Q(\mathbf{k}) & \mathcal{T} \\ \mathcal{T}^\dagger & \mathcal{H}_{SC}(\mathbf{k}) \end{pmatrix}.$$

In this representation, \mathcal{H}_Q is the Hamiltonian block corresponding to the quantum anomalous Hall insulator, \mathcal{H}_{SC} represents the Hamiltonian block for the superconductor, and \mathcal{T} signifies the coupling between them. Similar to the 2D case in the main text, the condition $\det[\mathcal{H}(\mathbf{k}=0)] = 0$ determines the phase boundary at which the holistic edge mode emerges or disappears. Using Schur Complement formula, the determinant can be decomposed as:

$$\det(\mathcal{H}) = \det(\mathcal{H}_{SC}) \cdot \det(\mathcal{H}_{Schur})$$

where the Schur complement, $\mathcal{H}_{Schur} \equiv \mathcal{H}_Q - \mathcal{T}\mathcal{H}_{SC}^{-1}\mathcal{T}^\dagger$. Given that the determinant of the superconductor

block satisfies $\det(\mathcal{H}_{SC}) > 0$, the topological condition $\det(\mathcal{H}) = 0$ equates to $\det(\mathcal{H}_{Schur}) = 0$. Through matrix algebra calculations, the Schur complement $\mathcal{H}_{Schur}(\mathbf{k})$ is:

$$\mathcal{H}_{Schur}(\mathbf{k}=0) = \begin{pmatrix} m\sigma_z - \mu_{\text{eff}} & i\Delta_{\text{eff}}\sigma_y \\ -i\Delta_{\text{eff}}\sigma_y & -m\sigma_z + \mu_{\text{eff}} \end{pmatrix},$$

where the effective chemical potential and the effective superconducting gap are $\mu_{\text{eff}} = \mu_m + \text{Re}(\chi)$ and $\Delta_{\text{eff}} = \text{Im}(\chi)$. These expressions rely on the auxiliary quantity χ , given by:

$$\chi = \sum_{k_z} \frac{|T_{k_z}|^2}{\epsilon(k_z) - i\Delta_s}, \quad \epsilon(k_z) = \frac{\hbar^2}{2m_s} k_z^2 - \mu_s.$$

Then the topological transition condition is obtained by $\det[\mathcal{H}_{Schur}(\mathbf{k}=0)] = 0$, which is Eq. (13) in the main text.

Appendix C—Usually, the low-energy effective Hamiltonian and the renormalization factor are derived using the Green's function method [30, 31]. Here, we propose an alternative approach based on the elimination method.

The eigenvalue equation for the system is given by:

$$\begin{pmatrix} \mathcal{H}_Q & \mathcal{T} \\ \mathcal{T}^\dagger & \mathcal{H}_{SC} \end{pmatrix} \begin{pmatrix} \psi_m \\ \psi_s \end{pmatrix} = E \begin{pmatrix} \psi_m \\ \psi_s \end{pmatrix}.$$

Eliminating ψ_s , we obtain the following equation in terms of ψ_m and E :

$$(\mathcal{H}_Q + \mathcal{T}(E - \mathcal{H}_{SC})^{-1}\mathcal{T}^\dagger)\psi_m = E\psi_m.$$

In the low-energy limit, where $E/\Delta_s \ll 1$, the energy E can be treated as a perturbation. Using a Taylor expansion, the term $(E - \mathcal{H}_{SC})^{-1}$ can be approximated as follows:

$$(E - \mathcal{H}_{SC})^{-1} = -\left(\mathbb{1} + \frac{E}{\mathcal{H}_{SC}}\right) \frac{1}{\mathcal{H}_{SC}},$$

where $\mathbb{1}$ denotes the unit matrix. Substituting this approximation into the previous equation yields the following:

$$(\mathbb{1} + \mathcal{T}\mathcal{H}_{SC}^{-2}\mathcal{T}^\dagger)^{-1}(\mathcal{H}_Q - \mathcal{T}\mathcal{H}_{SC}^{-1}\mathcal{T}^\dagger)\psi_m = E\psi_m.$$

Thus, the low-energy effective Hamiltonian is expressed as:

$$\begin{aligned} \mathcal{H}_L(\mathbf{k}) &= (\mathbb{1} + \mathcal{T}\mathcal{H}_{SC}^{-2}\mathcal{T}^\dagger)^{-1}(\mathcal{H}_Q - \mathcal{T}\mathcal{H}_{SC}^{-1}\mathcal{T}^\dagger) \\ &= Z \begin{pmatrix} h_Q(\mathbf{k}) - \mu_{\text{eff}} & i\Delta_{\text{eff}}\sigma_y \\ -i\Delta_{\text{eff}}\sigma_y & -h_Q^*(-\mathbf{k}) + \mu_{\text{eff}} \end{pmatrix}. \end{aligned}$$

Here, the renormalization factor Z is defined as $Z = \Delta_s/(\Delta_s + \Delta_{\text{eff}})$.